UNIVERSITY COLLEGE LONDON

DEPARTMENT OF PHYSICS & ASTRONOMY

Black Hole Shadows

MSc Research Essay

Samuel Lai

Supervised By:
Dr. Ziri YOUNSI and Prof. Kinwah WU

March 27, 2019

Abstract

A large ongoing international effort is currently under way to produce the first direct image of a supermassive black hole. Black hole shadows, which are the gravitationally lensed image of the unstable photon orbit boundary, are predicted to appear prominently in the image as a dark area over a bright background. Analysis of the size and shape of the shadow can reveal information about the black hole's physical parameters, such as its mass, angular momentum, and distance from the observer. In addition, information of the observer's orientation with respect to the black hole's rotation axis can also be obtained from the shape of the shadow. Using sub-millimeter wavelength Very-Long Baseline Interferometry (VLBI), I discuss the technical feasibility of observing Sagittarius A* (Sgr A*), our Galactic Center Supermassive Black Hole (SMBH) candidate. By using numerical simulations of black holes calculated with general-relativistic magnetohydrodynamics (GRMHD) and general-relativistic radiative transfer (GRRT), images of black holes with a variety of spin parameters are produced which predict the observed Sgr A* image. The dependence of the image on black hole and observer physical parameters is investigated and when the first black hole images are released in April 2019, these results can be compared to the simulated images presented here.

Contents

1 Introduction

Black holes are vacuum solutions to Einstein's field equations (Einstein, 1916). One year after Einstein published his equations, Karl Schwarzschild proposed a non-rotating spherically symmetric solution in 1916, called the Schwarzschild metric (Schwarzschild, 1916). The corresponding solution for a rotating, uncharged body, the Kerr metric, was not discovered until 1963 (Kerr, 1963). These solutions were considered mathematical curiosities and to this day, black holes have yet to be imaged directly. However, inferences from a number of independent lines of evidence have provided compelling evidence for the existence of black holes in nature. Observations of stellar orbits around the Milky Way Galactic Center provided measurements describing a massive, highly dense object which is inconsistent with any realistic stellar cluster (e.g., Ghez et al., 1998). Studies of accreting Active Galactic Nuclei (AGNs) have found highly efficient radiation from accretion disks matching the predictions made for rotating black holes (e.g., Bian and Zhao, 2003). As recently as 2016, multi-messenger astronomy with gravitational waves has provided another avenue of study into the effects of merging black holes (Abbott, 2016). The transient signal detected by the Laser Interferometer Gravitational-Wave Observatory (LIGO) matched the waveform predicted for black hole merger events. Despite this, it is said that, without a direct image, there is still no unambiguous proof that these objects are indeed black holes rather than some extra dense, pressure-supported configuration such as a dark star (Falcke, Melia, and Agol, 2000).

Today, a number of modern collaborations such as the Event Horizon Telescope (EHT) and BlackHole-Camera (BHC) projects are currently working towards imaging supermassive black holes for the first time. In particular, the EHT is expected to produce an image of the immediate environment of Sgr A* and Messier 87 (M87), soon to be released in April 2019.

This research essay will be on simulating images of rotating black holes using GRMHD and GRRT. The first sections of the essay will provide an overview of black holes, the GRMHD equations, and the radiation processes involved in GRRT. Next, discussion will revolve around the shadows which the black holes cast on the observer plane and how their shape depends on physical parameters associated with the black hole and the observation inclination angle. Suggestions will be made for how these effects can be disentangled to estimate the black hole mass and spin. Finally, this essay will investigate the observation methods used by the EHT collaboration and discuss some of the challenges associated with directly imaging black holes and the reconstruction of the image.

1.1 Black Holes

A black hole is an object predicted by Einstein's theory of general relativity which can be categorised by three physical quantities: mass, spin, and charge. Mass is an essential property, but since the spin and charge can vary, there exists four classifications of black holes as indicated in Table 1.

	No Spin (J = 0)	Spin (|J| > 0)
Uncharged (Q = 0)	Schwarzschild	Kerr
Charged (Q ≠ 0)	Reissner-Norström	Kerr-Newman

Table 1: *Black hole solutions of the Einstein field equations categorised by charge and spin.*

Schwarzschild black holes are the simplest solution with no spin or electrical charge, but due to the stellar evolutionary pathway which leads to the formation of a black hole, it is expected for black holes to retain some angular momentum from their progenitors. Charged black holes, while theoretically possible, are likely to be short-lived in nature, because they would quickly reach charge neutrality in the presence of surrounding plasma, as is expected for accreting black holes. Therefore, out of these four types, the most astrophysically-relevant solution is the Kerr black hole with $|J| > 0$ (Bardeen, Press, and Teukolsky, 1972).

Although a Kerr black hole is not charged, magnetic field lines develop from the charged plasma in an accretion disk. Through the Blandford-Znajek process (Blandford and Znajek, 1977), rotational kinetic energy can in principle be extracted from a spinning black hole within the ergosphere. Angular momentum transfer from the black hole to the accreting matter can also occur through the Penrose process (Penrose and M. Floyd, 1971). The result of these processes is that black holes with accretion disks have strong magnetic fields which power accretion dynamics.

Eddington Luminosity and Mass Accretion Rate

A spherically symmetric accreting system can be described by the net force (Frank, King, and Raine, 2002)

$$F_{\rm net} = \left(\frac{GM(m_{\rm p} + m_{\rm e})}{r^2}\right) - \frac{S\,\sigma_{\rm T}}{c}, \tag{1}$$

where S is the radiant energy flux and $\sigma_{\rm T}$ is the Thomson cross-section. The mass of the central body is M, while the speed of light is represented by c, and G is the gravitational constant. The mass of the proton and electron are represented by $m_{\rm p}$ and $m_{\rm e}$ respectively. Due to the spherically symmetric property of this accreting system, the net force is dependent only on the radius r from the central mass. The quantity, $S\sigma_{\rm T}/c$ is the outward radial force on an electron. For this system, hydrogen is assumed to be fully ionized and the radiation is assumed to exert a force on free electrons through Thomson scattering. SI units were employed for clarity. In hydrostatic equilibrium, the radiation force and the gravitational force balances so that $F_{\rm net} = 0$. By spherical symmetry, the luminosity is related to radiant energy flux as $L = 4\pi r^2 S$. In this system, the luminosity can be written as

$$L_{\rm Edd} \equiv L = \frac{4\pi GMm_{\rm p}c}{\sigma_{\rm T}} \approx 3.2\times 10^4 \left(\frac{M}{M_\odot}\right) L_\odot\,, \tag{2}$$

where $M_\odot$ is the solar mass and $L_\odot$ is the solar luminosity. This quantity is defined as the Eddington luminosity, which describes the maximum luminosity of a source in hydrostatic equilibrium. If the source has greater luminosity than the Eddington upper limit, the source body loses material by radiation outflow. In the context of Kerr black holes, the Eddington luminosity sets an upper limit on the radiation emitted from processes in its surrounding accretion disk.

The mass accretion rate is related to the luminosity by

$$L_{\rm acc} = \eta\dot{M}c^2, \tag{3}$$

where η is the nominal efficiency of converting accretion mass into energy and $\dot{M}$ is the mass accretion rate. The Eddington mass accretion rate corresponding to the Eddington luminosity is

$$\dot{M}_{\rm Edd} = \frac{10\,L_{\rm Edd}}{c^2}, \tag{4}$$

where the chosen value of $\eta = 0.1$ is a realistic value for highly efficient radiation as in accretion disks around black holes (Frank, King, and Raine, 2002). For a thin disk accretion model to apply, the mass accretion rate must be less than the Eddington rate, otherwise, the accreting material becomes too optically thick for the radiation to escape.

Kerr Black Holes

Unless otherwise stated in the subsequent discussion, geometric units are adopted such that $c = G = 1$ and the metric signature is [-,+,+,+]. In Boyer-Lindquist coordinates, the Kerr black hole line element is (Cunningham and Bardeen, 1973)

$$\begin{aligned} {\rm d}s^2 =& -(1 - 2Mr/\Sigma)\,{\rm d}t^2 - (4{\rm Ma\,r}\sin^2\theta/\Sigma)\,{\rm d}t\,{\rm d}\phi \\ &+ (\Sigma/\Delta){\rm dr}^2 + \Sigma\,{\rm d}\theta^2 + ({\rm r}^2 + {\rm a}^2 + 2{\rm Ma}^2\sin^2\theta/\Sigma)\sin^2\theta\,{\rm d}\phi^2, \end{aligned} \tag{5}$$

where the functions Σ and Δ are defined as

$$\Sigma \equiv r^2 + a^2 \cos^2\theta, \qquad \Delta \equiv r^2 - 2M\,r + a^2. \tag{6}$$

The dimensionless black hole spin parameter a, also called the “Kerr parameter”, is the angular momentum per unit mass, and is defined as $a \equiv cJ/(GM^2)$, where M is the black hole mass and J is the angular momentum. Its maximum value is $a = 1$, where if the black hole spin is above this value, the event horizon does not form and the black hole singularity is in principle visible to external observers. The existence of these naked singularities have important theoretical implications, including a violation of causality under general relativity, but although several mechanisms have been proposed to form superspinning Kerr black holes, they have yet to be observed (Chakraborty, Kocherlakota, and Joshi, 2017). By conservation of angular momentum, ejected matter causes the black hole to lose angular momentum, lowering its spin parameter. In reality, the loss of angular momentum to ejected matter is inconsequential over observation time-scales of interest, such as the mean human life-span, so the spin parameter is assumed to be time-invariant in the GRMHD simulation described in Section 2.

Under the Boyer-Lindquist coordinates, the metric is divergent when $\Delta = 0$. Setting Δ in eqn. (6) to zero, the positive root of r defines the radius of the event horizon,

$$r_{\mathrm{EH}} \equiv M + (M^2 - a^2)^{1/2}, \tag{7}$$

where M is the mass of the black hole. The event horizon is independent of the θ, ϕ angular coordinates and the classical Schwarzschild radius $r_{\mathrm{s}} = 2M$ can be obtained in the limit that $a = 0$. However, this event horizon is a coordinate singularity which can be removed by a different choice of coordinates. Instead, it can be shown in Kerr-Schild coordinates that the Kerr physical singularity is a ring of zero thickness located on the equatorial plane (Visser, 2007).

The static limit is located where the g_{tt} component of the Kerr metric vanishes. Consequently time-like world-lines outside the static limit turn into space-like world-lines. Reading g_{tt} from the metric in eqn. (5), the positive root of the equation $(\Sigma - 2Mr) = 0$ is given by

$$r_{\mathrm{SL}} \equiv M + \left(M^2 + a^2\, \cos^2\theta\right)^{1/2}, \tag{8}$$

where there is a dependence on θ. Inside the region bounded by the static limit, called the ergosphere, spacetime is dragged in the black hole's direction of rotation. This is called the rotational frame-dragging or the Lense-Thirring effect (Thirring, 1918). Photon trajectories plotted in Fig. 4 show frame-dragging at work.

The Lagrangian can be written from the Kerr metric by the general formula derived from the principle of least action,

$$\mathcal{L} = \frac{1}{2} g_{\mu\nu} \dot{x}^\mu \dot{x}^\nu, \tag{9}$$

where $g_{\mu\nu}$ denotes the metric element and the Greek indices take on the values 0, 1, 2, or 3, such that x^μ represents a position four-vector and the dotted $\dot{x}^\mu$ is its derivative with respect to an affine parameter chosen to parameterise the path, i.e. proper time. From Noether's theorem, if the Lagrangian is invariant under modifications of a quantity, then there is an associated conserved quantity. The Kerr black hole Lagrangian is independent of time t and angle ϕ, suggesting that the energy and angular momentum are conserved. In general relativity, Killing vectors are defined such that the Lie derivative of the Killing vector field vanishes and these can similarly be used to express symmetries in the geometry of spacetime which preserve the metric (D'Inverno, 1992). The t and ϕ vectors are Killing vectors for the Kerr metric associated with the conserved quantities

$$E = -p_{\mathrm{t}}, \qquad L = p_\phi, \tag{10}$$

where E is the total energy, and L is the angular momentum parallel to the spin axis. A third conserved quantity called the Carter's constant comes from Killing tensor field, instead of a Killing vector, and expresses a higher order symmetry (Carter, 1968). The Carter constant is defined as

$$Q = p_\theta^2 + \cos^2\theta \, \left[a^2 \left(\mathrm{m}^2 - \mathrm{p}_\mathrm{t}^2\right) + \mathrm{p}_\phi^2 \mathrm{csc}^2\theta\right], \tag{11}$$

where Q, the Carter's constant, corresponds to the total angular momentum plus a precisely determined additional term quadratic in linear momenta (Rosquist, Bylund, and Samuelsson, 2009). The particle rest mass is represented by m and the generalized momenta, p_i are defined by Lagrangian mechanics in terms of generalized positions q_i with the differential $p_\mathrm{i} = \partial\mathcal{L}/\partial\dot{q}_\mathrm{i}$. In the Schwarzschild limit with $\theta = \pi/2$, the Carter's constant reduces to the orbital angular momentum squared. The fourth conserved quantity of motion, the particle rest mass, is related to the invariance of the line element under transformation. The contraction of the four-momentum is $p^\mu p_\mu = -m^2$, where $m = 0$ for massless particles such as photons. Hereafter, formulae which appear with upper and lower signs (ie.±) represent prograde and retrograde orbits respectively. Using the Euler-Lagrange formalism, the equations of motion governing orbital trajectories around the Kerr black hole are

$$\begin{aligned}
\Sigma\frac{dr}{d\lambda} &= \pm(V_\mathrm{r})^{1/2},\\
\Sigma\frac{d\theta}{d\lambda} &= \pm(V_\theta)^{1/2},\\
\Sigma\frac{d\phi}{d\lambda} &= -(a\,E - L/\sin^2\theta) + \mathrm{a\,T}/\Delta,\\
\Sigma\frac{dt}{d\lambda} &= -a\,(a\,E\sin^2\theta - \mathrm{L}) + (\mathrm{r}^2 + \mathrm{a}^2)\mathrm{T}/\Delta,
\end{aligned} \tag{12}$$

where λ is an affine parameter related to the proper time τ by $\lambda = \tau/m$. The effective potentials governing the motion in the r and θ coordinates are

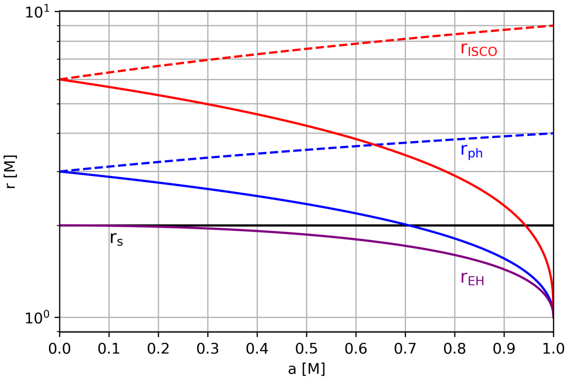

Figure 1: *Kerr black hole critical radii. The solid and dashed lines mark the critical radii for prograde and retrograde rotation respectively. This figure was created using eqns. (7), (15), and (16).*

$$\begin{aligned}
V_\mathrm{r} &\equiv T^2 - \Delta\,[m^2 r^2 + (L - a\,E)^2 + Q],\\
V_\theta &\equiv Q - \cos^2\theta[\mathrm{a}^2\left(\mathrm{m}^2 - \mathrm{E}^2\right) + \mathrm{L}^2/\sin^2\theta],
\end{aligned} \tag{13}$$

where the potentials are functions only of r and θ, whereas $T \equiv E(r^2 + a^2) - a\,L$. Considering circular orbits satisfy the condition $dr/d\lambda = 0$, it is then possible to solve for the conserved quantities E and L in terms of r, spin a, and black hole mass M to give

$$\begin{aligned}
E/m &= \frac{r^{3/2} - 2M\,r^{1/2} \pm aM^{1/2}}{r^{3/4}\,\left(r^{3/2} - 3M\,r^{1/2} \pm 2aM^{1/2}\right)^{1/2}},\\
L/m &= \frac{\pm M^{1/2}\left(r^2 \mp 2aM^{1/2}\,r^{1/2} + a^2\right)}{r^{3/4}\left(r^{3/2} - 3M^{1/2}\,r^{1/2} \pm 2aM^{1/2}\right)^{1/2}}.
\end{aligned} \tag{14}$$

The formulae for energy and angular momentum parallel to the rotation axis in eqn. (14) share a common denominator which is only real when the expression in the square root is positive. The limiting case when $\left(r^{3/2} - 3r^{1/2} \pm 2a\right) = 0$ describes the boundary for a region of space in which circular orbits do not exist for particles with non-zero mass. Only massless particles such as photons can maintain an unstable orbit on this boundary (Bardeen, Press, and Teukolsky, 1972). Hereafter referred to as unstable photon orbit and r_ph, its radius is defined as

$$r_\mathrm{ph} = 2M\left\{1 + \cos\left[\frac{2}{3}\cos^{-1}\left(\mp\mathrm{a}\right)\right]\right\}. \tag{15}$$

For a spinning black hole $a \neq 0$, there is a different radius for prograde (negative sign) and a retrograde (positive sign) unstable photon orbits. Another important critical radius is the innermost stable circular orbit (ISCO), which marks the inner radius of a black hole accretion disk. Stability requires the condition that the second derivative of the radial potential is negative or zero, that is $V_{\mathrm{r}}''(r) \leq 0$. This radius can be calculated from the spin parameter by the equations:

$$\begin{aligned} r_{\mathrm{ISCO}} &= M\left(3 + Z_2 \mp [(3 - Z_1)(3 + Z_1 + 2Z_2)]^{1/2}\right), \\ Z_1 &\equiv 1 + (1 - a^2)^{1/3}\left[(1 + a)^{1/3} + (1 - a)^{1/3}\right], \\ Z_2 &\equiv \sqrt{3a^2 + Z_1^2}. \end{aligned} \tag{16}$$

As the spin of the black hole increases, the retrograde ISCO increases towards $9\,r_{\mathrm{g}}$, where $r_{\mathrm{g}} = GM/c^2$ is the gravitational radius, but the prograde ISCO radius and innermost photon circular orbit radius decrease towards the black hole event horizon for a maximally spinning black hole. Fig. 1 compares the prograde and retrograde ISCO, unstable photon orbit, and event horizon radii for a Kerr black hole.

2 General-Relativistic Magnetohydrodynamics

Kerr black holes are characterized by rotation along with strong gravitational and electromagnetic fields. To understand their structure, it is useful to adopt an ideal GRMHD model, treating the plasma as a perfect electrically conducting fluid. The advantages of ideal GRMHD in comparison to alternative semi-analytic models is that rather than calculating through the equations of motion for each particle, the system can be described by a single conducting fluid with associated macroscopic quantities such as pressure and density. Ideal GRMHD assumes a single component fluid of ions with no distinctions between species. The effects of radiative cooling are neglected and the perfect fluid has an ideal equation of state with isotropic pressure, completely characterized by its rest frame mass density.

2.1 Equations of General-Relativistic Magnetohydrodynamics

The ideal equation of state defines the relationship between density and gas pressure in a thermodynamic system. Under the calorically perfect gas approximation which obeys the ideal-gas law and has temperature-independent heat capacities, the relationship between density ρ and gas pressure P is written as

$$P = (\gamma - 1)\rho e, \tag{17}$$

where the ratio of specific heats $\gamma = C_{\mathrm{p}}/C_{\mathrm{v}}$, called the adiabatic index, is equal to 5/3 for non-relativistic monatomic fluid and 4/3 for monatomic relativistic fluid. The internal energy per unit mass is written as $e = C_{\mathrm{v}}T$.

GRMHD is numerically integrated with a conservative scheme. The particle number and mass are conserved quantities (Gammie, McKinney, and Toth, 2003), which follow the conservation law

$$(nu^{\mu})_{;\mu} = 0\,, \tag{18}$$

where n is the particle number density and u^{μ} is the four-velocity. The notation involving the semi-colon subscript is used to denote a covariant derivative, ${V^{\nu}}_{;\mu} = \nabla_{\mu}V^{\nu}$.

The conservation of energy-momentum including all contributions by the perfect fluid and electromagnetic field can be written succinctly as

$${T^{\mu\nu}}_{;\nu} = 0\,. \tag{19}$$

The fluid part of the stress-energy tensor depends on the internal energy U, pressure P, and density ρ in the form

$$T^{\mu\nu}_{\mathrm{fluid}} = (\rho + U + P)\,u^{\mu}u^{\nu} + Pg^{\mu\nu}. \tag{20}$$

Ideal MHD simplifies the generalized Ohm's law, neglecting resistivity, anisotropy, electron inertia, and the

Hall term proportional to $J \times B$, obeying the relationship

$$E + v \times B = 0. \tag{21}$$

In the rest frame of the fluid, the electric field goes to zero because of the high conductivity of the fluid. Thus, the electromagnetic part of the stress-energy tensor can be written as

$$T^{\mu\nu}_{\text{EM}} = b^2 u^\mu u^\nu + \frac{1}{2} b^2 g^{\mu\nu} - b^\mu b^\nu, \tag{22}$$

where b^μ is a magnetic field four-vector written in Lorentz-Heaviside units and defined as

$$b^\mu \equiv -\frac{1}{2} \epsilon^{\mu\nu\kappa\lambda} u_\nu F_{\lambda\kappa}, \tag{23}$$

with $F^{\mu\nu}$ representing the electromagnetic field tensor and $\epsilon^{\mu\nu\kappa\lambda}$ is the Levi-Civita tensor. Evolution of the electromagnetic field is governed by Maxwell's equations and the conserved Faraday tensor,

$$F^{\mu\nu}{}_{;\mu} = 0. \tag{24}$$

In Lorentz-Heaviside units, factors of 4π no longer appear explicitly in Maxwell's equations. Altogether, the full conserved stress-energy tensor for the system is the sum of the fluid and electromagnetic parts,

$$\begin{aligned} T^{\mu\nu}_{\text{MHD}} &= T^{\mu\nu}_{\text{EM}} + T^{\mu\nu}_{\text{fluid}} \\ &= \left(\rho + U + P + b^2\right) u^\mu u^\nu + \left(P + \frac{1}{2} b^2\right) g^{\mu\nu} - b^\mu b^\nu. \end{aligned} \tag{25}$$

2.2 Implementation

The GRMHD simulation proceeds by taking discrete time steps while updating a set of conserved variables and a set of "primitive" variables, which are used to model the accretion flow. The conserved variables are calculated with fluxes across a meshed geometry using the finite volume method (Porth et al., 2017). This converts all volume integrals containing divergence terms into surface integrals by the divergence theorem. There exists an analytic function relating the primitive variables to the conserved variables, but inverting the relationship requires a multi-dimensional Riemann solver.

The initial conditions of the simulation contain the Fishbone-Moncrief magnetised torus (Fishbone and Moncrief, 1976) supported by centrifugal and pressure forces, wherein magneto-rotational instability (MRI) develops after an initial perturbation of the magnetic field in the torus. MRI provides the turbulent stresses and angular momentum transfer between particles connected by magnetic field lines (Balbus and Hawley, 1991). The effect leads to an amplification of the magnetic field, which drives accretion onto the black hole. Over time, the accretion flow reaches a quasi-stationary state characterised by equilibrium between the in-flow and out-flow of material.

2.3 Accretion Flow Structure

While in the quasi-stationary state, distinct regions of the black hole accretion disk can be identified by the mass density ρ, magnetisation σ, and plasma beta β profiles. The magnetisation represents the density of magnetic moments and is expressed as

$$\sigma \equiv \frac{b^2}{\rho}, \tag{26}$$

where $b^2 = b^\mu b_\mu$ is a contraction of the magnetic field four-vector. The plasma beta is a ratio of the plasma and magnetic pressure

$$\beta \equiv \frac{P_{\text{gas}}}{P_{\text{mag}}}, \tag{27}$$

where $P_{\text{gas}} = nk_{\text{B}}T$ and $P_{\text{mag}} = b^2/2$. The ratio indicates whether it is the field which drags the plasma motion for small plasma beta, or the plasma drags the field for large plasma beta.

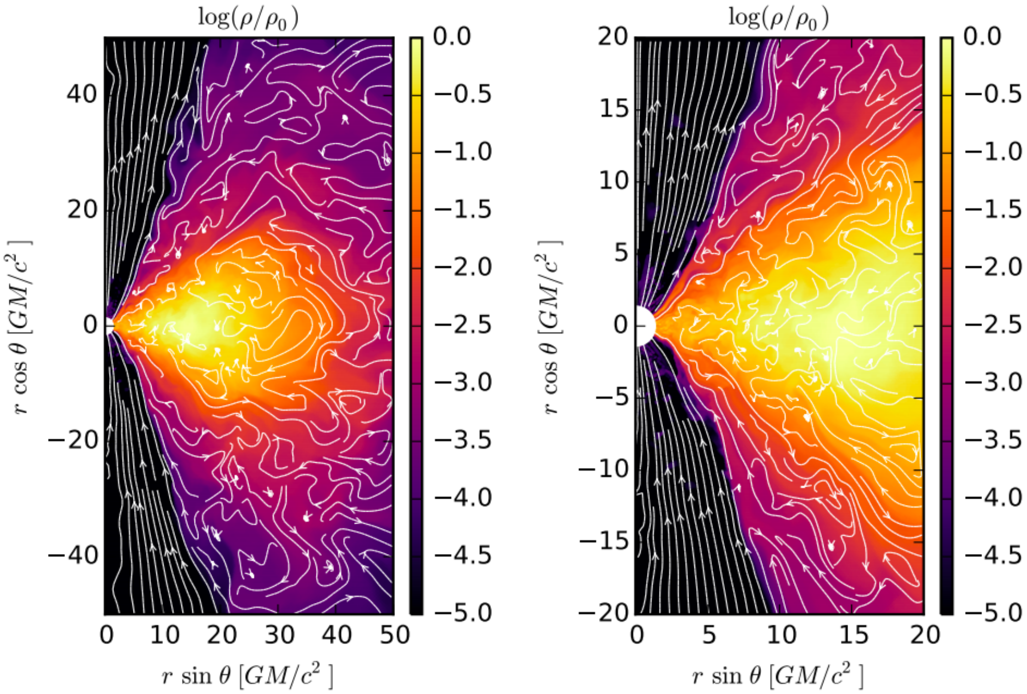

Figure 2: *Schematic showing a cross-sectional slice of the magnetised torus where the black hole spin parameter is 0.9375. The magnetic field lines are shown in white. The left panel shows the large scale accretion structure and the right panel is zoomed into the central region, where the white semi-circle indicates the radius of the event horizon. The figure clearly shows the distinct black hole accretion regions: disk (yellow), wind (orange and purple), and jet (black). Within the jet funnel, the magnetic field lines are ordered and point along the black hole rotation axis. In the wind and accretion disk, the magnetic field lines are turbulent. Figure is obtained from Goddi, 2016.*

After a long time-evolution of the GRMHD simulation, the disk reaches a quasi-stationary state. Near the poles of the black hole rotation axis is a low density outflow region characterized by jets of highly relativistic particles indicated by the dark region in Fig. 2. The jet is an evacuated region of low density characterised by a high magnetisation and low plasma beta. The accretion disk makes up the inflow region perpendicular to the rotation axis; it is characterized by high density, viscosity, plasma beta, and comparatively low magnetisation. The space between the optically thick disk and the low density jet has intermediate values for density, magnetisation, and plasma beta, but it is separated from the jet by a thin boundary called the sheath Goddi, 2016.

3 General-Relativistic Radiative Transfer

3.1 Radiative Transfer

The variation of specific intensity along a ray incorporates effects from emission and absorption (Rybicki and Lightman, 1986)

$$\frac{dI_\nu}{ds} = -\alpha_\nu I_\nu + j_\nu, \tag{28}$$

where I_ν is the specific intensity, α_ν is the absorption coefficient, and j_ν is the emission coefficient. The subscript ν indicates a dependence of each of these terms on the frequency.

By defining the optical depth $d\tau_\nu = \alpha_\nu ds$ and the source function as a ratio of the emission and absorption coefficients $S_\nu \equiv \frac{j_\nu}{\alpha_\nu}$, the radiative transfer equation can be rewritten as

$$\frac{dI_\nu}{d\tau_\nu} = -I_\nu + S_\nu, \tag{29}$$

where the following is a solution for the intensity at a specified optical depth if the source function is constant:

$$I_\nu(\tau_\nu) = S_\nu + \left(I_\nu(0) - S_\nu\right) e^{-\tau_\nu}. \tag{30}$$

In practice, the source function is not constant and must be solved numerically. Before the equation can be applied to black hole accretion disks, the radiative transfer equation must be written in covariant form for relativistic particles in arbitrary spacetime geometry (Younsi, Wu, and Fuerst, 2012). As photons have zero mass, the GRRT equation can be expressed as

$$\frac{d\mathcal{I}}{d\lambda} = -k_\beta u^\beta \bigg|_\lambda \left(-\alpha_{0,\nu} I_\nu + \frac{j_{0,\nu}}{\nu^3}\right), \tag{31}$$

where the Lorentz-invariant intensity $\mathcal{I}$ is related to specific intensity I_ν by $\mathcal{I} = I_\nu/\nu^3$. As indicated by the subscript "0", both $\alpha_{0,\nu}$ and $j_{0,\nu}$ are evaluated at the local rest frame of the fluid. Aberration terms resulting from the radiative transfer equation for particles with mass are ignored and the four-momentum of a massless particle is denoted by k_α. This formulation of the radiative transfer equation can be applied to calculate the emission from accreting spinning black holes.

3.2 Radiation Processes

Synchrotron and Bremsstrahlung

Accretion flows around Kerr black holes produce emission from accelerating charged particles (Luminet, 1979; Morgan et al., 2007) and are divided into cold or hot classes depending on the opacity of the disk (Yuan and Narayan, 2014). Cold accretion is optically thick with high mass accretion rates, sometimes close to the Eddington rate. They describe many of the luminous AGNs in the Universe. Hot accretion flows are optically thin with low radiative efficiency, similar to Sgr A*. Ionized plasma in magnetic fields, which are present around accreting black holes, produce bremsstrahlung and synchrotron radiation. However, relative to bremsstrahlung, synchrotron is expected to be the dominant mechanism for radiation in accretion disks around Kerr black holes because of the low number density in the accretion plasma. Synchrotron radiation is a single-body process scaling with one factor of the number density, whereas bremsstrahlung is a two-body process with a quadratic dependence on the number density (Abramowicz and Fragile, 2013). At the observation frequencies of interest in the sub-mm wavelength, the emission from the bremsstrahlung process is insignificant compared synchrotron emission. Therefore, the bremsstrahlung radiation is omitted in simulations of the accretion disk emission shown in Section 4.

For synchrotron radiation, free electrons are accelerated by magnetic fields, causing them to travel in helical trajectories described by a characteristic precessional Larmor frequency and radius (Rybicki and Lightman, 1986). For relativistic velocities, it is useful to define the velocity as $\beta \equiv v/c$ and the Lorentz factor $\gamma \equiv 1/\sqrt{1-\beta^2}$. The Larmor angular frequency is

$$\omega_{\mathrm{B}} = \frac{eB}{\gamma m_{\mathrm{e}} c}, \tag{32}$$

where B is the magnitude of the magnetic field, and e is the electron charge.The Larmor radius is

$$r_{\mathrm{L}} = \frac{\gamma m_{\mathrm{e}} c^2 \beta}{eB}, \tag{33}$$

The contribution of electrons to the radiation from the accretion disk is more significant than that of ions in the plasma because of their lower mass $m_{\mathrm{p}}/m_{\mathrm{e}} \approx 1836$, so electrons experience a greater acceleration and angular frequency in a tighter gyroradius. In the GRMHD simulation discussed in Section 2, protons and electrons are assumed to be thermally coupled by a fixed ratio related to temperature. This assumption is valid for slow-moving accretion flow near the accretion disk, because there is enough time for particles to interact. But this assumption is inaccurate for fast-moving, highly magnetised, and relativistic jets near the poles of the Kerr black hole. For Sgr A*, large scale jets are not observed and observations of Sgr A* fit multiple disk-dominated models (Issaoun, 2019). Therefore, the assumption of thermal coupling between the protons and electrons is acceptable.

Recalling the relativistic Larmor formula for the power radiated by an accelerated electron,

$$P = \frac{2e^2\gamma^6}{3c}\left[\dot{\beta}^2 - \left(\beta \times \dot{\beta}\right)^2\right], \tag{34}$$

the power output of the synchrotron radiation can be expressed as

$$P_{\mathrm{syn}} = \frac{4}{3}\sigma_{\mathrm{T}} c \beta^2 \gamma^2 U_{\mathrm{B}} \sin^2\alpha, \tag{35}$$

where U_{B} is the magnetic energy density and α is the pitch angle defined between the velocity β of the electron and the magnetic field direction.

Inverse Compton Scattering

Compton scattering is the inelastic collision and subsequent exchange of energy and momentum between particles and photons, where usually the interaction is between an electron and a photon. Forward Compton scattering is when part of the photon's energy is transferred to the electron, which increases the photon wavelength. The relationship between the change in wavelength, $\Delta\lambda$, in relation to the scattering angle, θ, is described by

$$\Delta\lambda = \frac{h}{m_{\mathrm{e}} c}\left(1 - \cos\theta\right), \tag{36}$$

where h is the Planck constant, and θ is the scattering angle. The quantity $h/m_{\mathrm{e}}c$ is called the Compton wavelength.

In inverse Compton scattering, photons are up-scattered by highly relativistic electrons and gain significant energies, shifting them to higher frequencies. This can be seen in the full spectral energy distribution (SED) of Sgr A*, Fig. 8, where local maxima in flux density appear at high frequencies between 10^{13} and 10^{18} Hz. The higher frequency peaks show that photons around the 600 GHz global flux density maximum have been up-scattered to higher energies; these are sometimes called Comptonized photons. As seen in Fig. 8, the Comptonized photons can be neglected for EHT observations made in the 230 GHz frequency band, denoted by the highlighted region, so these effects are not considered in Sections 2 and 4.

A similar relation to the synchrotron power output in eqn. (35) can be written for inverse Compton scattering by replacing the magnetic energy density with the radiation field energy density, U_{rad}, obtaining

$$P_{\mathrm{IC}} = \frac{4}{3}\sigma_{\mathrm{T}} c \beta^2 \gamma^2 U_{\mathrm{rad}}, \tag{37}$$

where the expression is valid for the scattering of a single electron.

3.3 Transforming From Code to Physical Units

Physical quantities in the code are derived from the choice of $M_{\mathrm{BH}} = 1$, which determines the characteristic length scale and time scale in the system. The length scale is equivalent to the gravitational radius $L_{\mathrm{unit}} = r_{\mathrm{g}}$ and the time-scale is related to the light-crossing time $t_{\mathrm{unit}} = r_{\mathrm{g}}/c$. Then, the mass unit is equal to the mass accretion rate in normal centimetre-gram-second (cgs) units multiplied by the time-scale $M_{\mathrm{unit}} = \dot{M}_{\mathrm{cgs}} \times t_{\mathrm{unit}}$. The physical mass accretion rate in cgs units, $\dot{M}_{\mathrm{cgs}}$, is a free parameter set as an initial condition to achieve a desired flux at a certain frequency. Further explanation is provided in Section 4.

The density scale is a combination of the previously defined units $\rho_{\rm unit} = M_{\rm unit}/L_{\rm unit}^3$ and the number density is related to the density by assuming the plasma is composed purely of ionized hydrogen $n_{\rm unit} = \rho_{\rm unit}/(m_{\rm e} + m_{\rm p})$. The code units for the square of the magnetic field strength is represented by $B^2 = c^2\rho_{\rm unit}(m_{\rm e} + m_{\rm p})$. To convert code units into physical units related to observation, dimensionless quantities can be rescaled back into cgs quantities. The magnetisation is one such example where $\sigma = b_{\rm code}^2/\rho_{\rm code} = b_{\rm cgs}^2/\rho_{\rm cgs}$, such that multiplying the value of magnetisation obtained in the code units by the density in cgs units would result in the square of the magnetic field strength in cgs units. Similarly, gravitational radii can be converted into an angular size; observing Sgr A* with an estimated mass of $M_{\rm BH} \approx 4.5 \times 10^6 M_\odot$ and an observing distance of $d = 8.5 \times 10^3\,{\rm pc}$, one gravitational radius scales with angular size as $1\,r_{\rm g} \approx 5.29\,\mu{\rm as}$. This result is used in Figs. 6, 7, and 10 to scale the simulated images to the angular size of Sgr A*.

4 Black Hole Shadow

It has been predicted for many years (e.g., Luminet, 1979; Falcke, Melia, and Agol, 2000) that black holes cast a "shadow" against the background sky, as seen by a distant observer. In particular, the properties of the shadow depend sensitively on the black hole mass and spin, as well as the terrestrial observer's orientation with respect to the black hole.

In the general-relativistic description of a Schwarzschild black hole, the aforementioned unstable photon orbit defines the region of space where photons are forced to travel unstable circular orbits at its boundary. For Kerr black holes, the unstable photon orbits precess and are dependent on the angle of orbit around the rotation axis. Due to the orbital instability, perturbations on the photon cause it to either fall into the black hole or escape. Inside the region bounded by unstable orbits, photons are unable to escape the black hole's gravitational potential, but photons outside can escape and reach distant observers. The black hole shadow can be defined as the geometric projection of the unstable photon orbit boundary onto the observer plane (Dokuchaev and Nazarova, 2018). Observationally, the black hole shadow can appear as a dark axisymmetric region within a bright background (Repin et al., 2018).

For a Schwarzschild black hole, the impact parameter, b, defining the radius of the black hole shadow is a constant $b = \sqrt{27}M$ (Shaikh et al., 2019). However, the shadow radius for a Kerr black hole has a dependence on the spin of the black hole itself and the observer's inclination angle; whereas the mass of the black hole determines the absolute size of the shadow rather than its shape. The same effect occurs when varying the observer's distance closer to or further from the black hole. When the observer is moved closer, the size of the shadow appears larger, such that the black hole mass appears greater. Similarly when the observer is moved further away, the size of the shadow shrink and the black hole mass appears lower. The shape of a Kerr black hole shadow is well-defined by its physical parameters and can be described by an analytical solution (e.g., Grenzebach, Perlick, and Lämmerzahl, 2014; Shaikh et al., 2019). In vacuum, the analytical form can be written in Cartesian coordinates as (Grenzebach, Perlick, and Lämmerzahl, 2014)

$$\begin{aligned} x(r_{\rm p}) &= -2\tan\left(\frac{\theta(r_{\rm p})}{2}\right)\sin\left(\Psi(r_{\rm p})\right), \\ y(r_{\rm p}) &= -2\tan\left(\frac{\theta(r_{\rm p})}{2}\right)\cos\left(\Psi(r_{\rm p})\right), \end{aligned} \tag{38}$$

where $\theta(r_{\rm p})$ and $\Psi(r_{\rm p})$ are celestial coordinates and functions of the radius parameter. The celestial coordinates are spherical coordinates defined for the observer by the tangent vector

$$\dot{\lambda} = \alpha\left(-e_0 + \sin\theta\cos\Psi e_1 + \sin\theta\sin\Psi e_2 + \cos\Psi e_3\right), \tag{39}$$

where α is a scalar factor and each light ray $\lambda(s)$ has a coordinate representation $(t(s), r(s), \vartheta(s), \phi(s))$. The set of coordinates (e_0, e_1, e_2, e_3) are an orthonormal tetrad chosen to describe the time and position of the observation event.

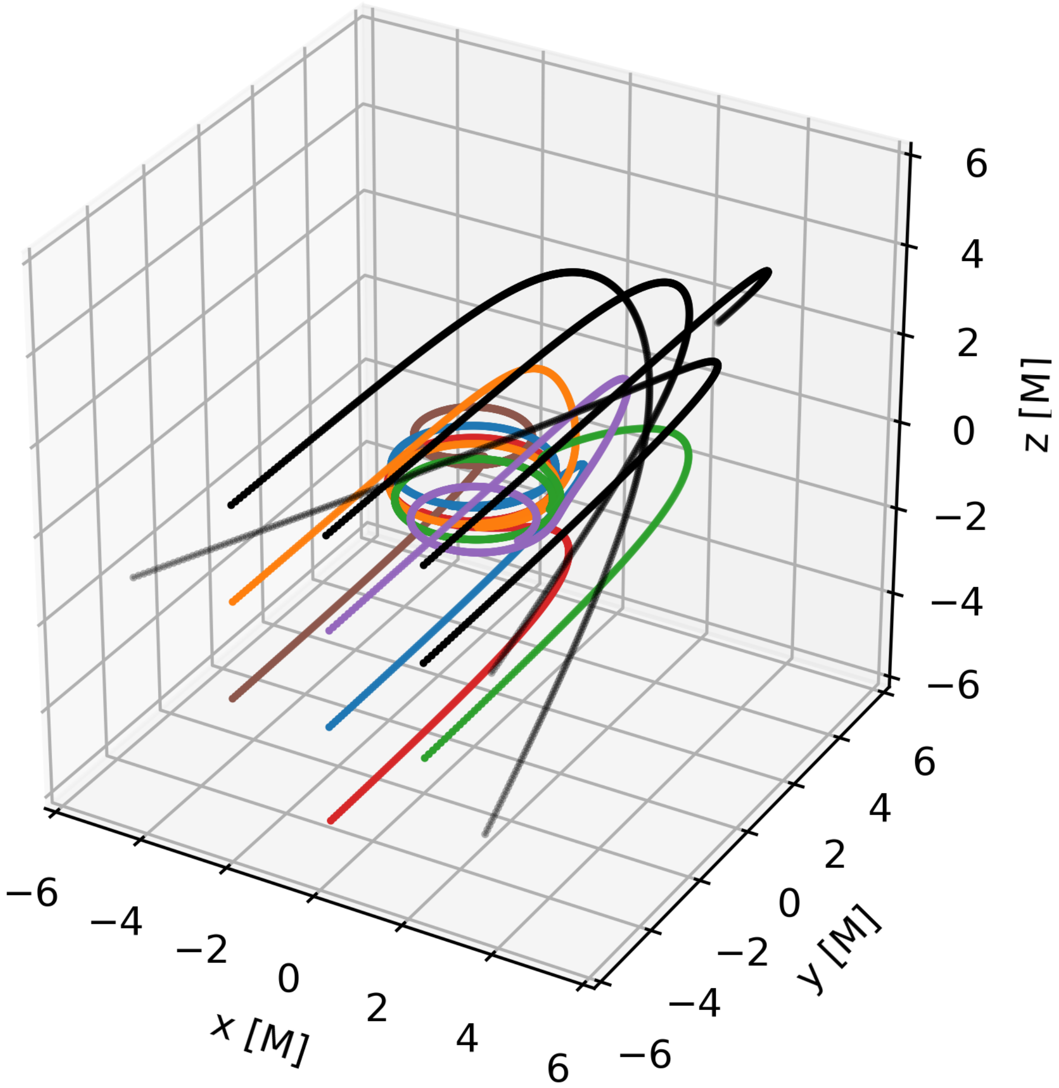

Figure 3: *Three-dimensional plot displaying photon trajectories where coloured paths represent photons captured by the black hole and black paths represent escaping photons. The black hole spin parameter is 0.9375 (close to maximal spin). The trajectories was calculated from vacuum integration of geodesics around the black hole spacetime as part of the GRRT routine.*

The method used to obtain the black hole shadow in Section 4 is to use vacuum integration of geodesics around the Kerr black hole curved spacetime and perform reverse ray tracing from the distant observer to the black hole, noting when the photon is captured or can escape. This is shown in Fig. 3 and Fig. 4, with the observer placed at a distance of $r = 1000\,r_{\rm g}$. The three-dimensional boundary between the captured and escaping photons defines the photon sphere, which can be seen as the region of space bounded by the coloured photon trajectories in Fig. 3.

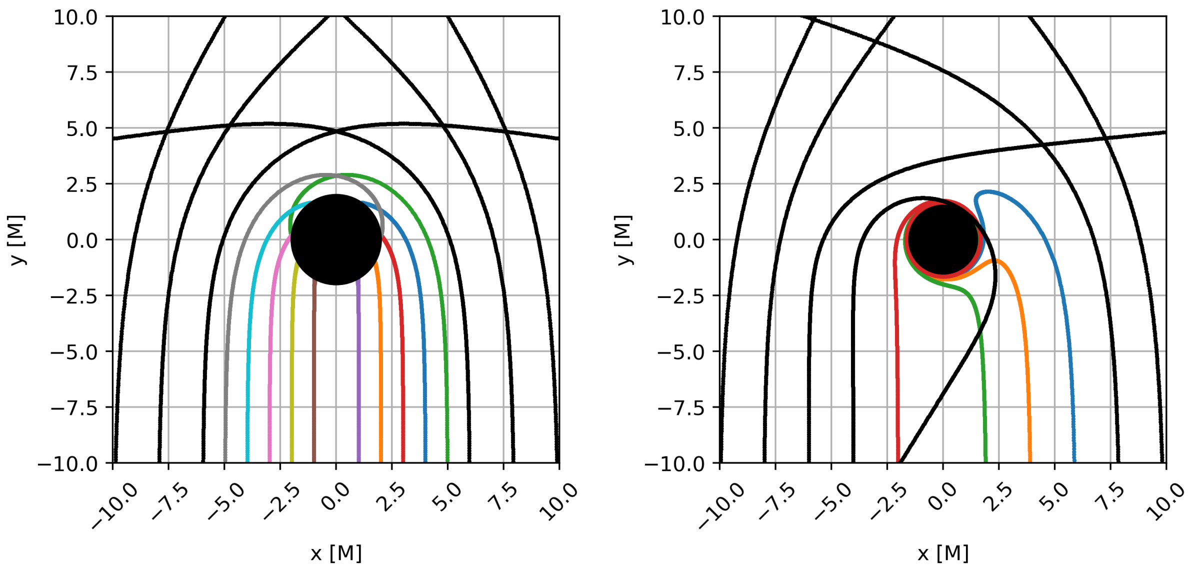

Figure 4: *Two-dimensional plot of photon trajectories where coloured paths represent photons captured by the black hole and black paths represent escaping photons. The central black circle indicates the extent of the event horizon. The black hole in the left panel has a spin parameter of 0 and in the right panel, the spin parameter is 0.9375, hence the left-right asymmetry. The right panel shows the Lense-Thirring effect, where incoming photons in the counter-rotating direction are dragged into the same direction of rotation as the black hole within its ergosphere, whereas the left panel shows symmetric trajectories between the left and right rays. The trajectories were computed from vacuum integration of geodesics around the black hole spacetime as part of the GRRT routine.*

One of the parameters affecting the shape of the black hole shadow is the black hole's spin. As the spin increases, the shadow becomes more asymmetric due to frame-dragging and the height of the shadow along the rotation axis is affected by the observer's inclination angle.

By disentangling the effects of spin and observer's inclination angle on the shadow shape, it is theoretically possible to infer the black hole's physical parameters. The extent of the displacement in the shadow from the rotation axis is largely dependent on the spin (Li and Bambi, 2014), but the position of the rotation axis is difficult to determine observationally. Furthermore, black hole shadows of similar size and shape can be found for a variety of black hole mass and spin parameters. This degeneracy of parameters makes inferring spin from shape of the black hole shadow impractical. However, if the position of the black hole mass center can be determined, it is possible to measure the spin parameter by defining a *shadow axis* which can be observationally determined (Takahashi, 2004). The details of this method are described in Section 4.3.

Apart from observationally measuring the black hole physical parameters, the black hole shadow may also be used as a way to test general relativity against alternative theories of gravity. However, with current available methods and observations of Sgr A* shadow at 230 GHz alone, the results show that it is difficult to distinguish Kerr and dilation black hole spacetimes (Mizuno et al., 2018). More advanced image reconstruction methods, expansion of observation bandwidth and frequency, as well as the addition of telescopes to VLBI will improve the ability to test general relativity against alternative theories by observing black hole shadows.

4.1 Shape of the Black Hole Shadow

In the left panel of Fig. 5, the shadow asymmetry grows with increasing spin in a direction that depends on prograde or retrograde rotation, but the vertical width of the shadow does not vary. In the right panel, the height of the shadow expands with increasing observer inclination angle. Shadows of negatively spinning black holes are asymmetric in the opposite direction compared to shadows of positively spinning black holes, but the major and minor axis of the black hole shadow are equivalent for spins of a different sign with the same magnitude. Furthermore, a Schwarzschild black hole shadow is circular when viewed from any inclination angle, whereas a spinning black hole shadow is circular only when observed along the rotation axis. This information can be used to infer physical properties from observations of black hole shadows, discussed in Section 4.3.

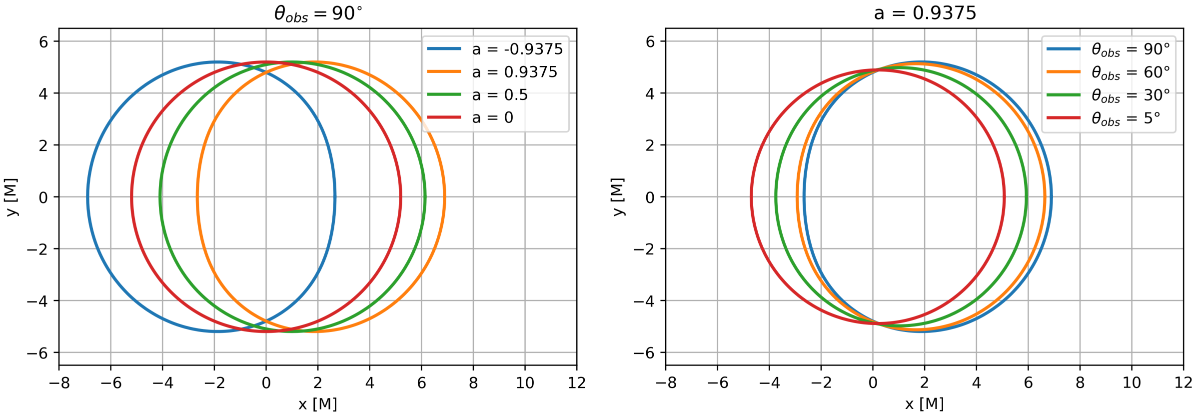

Figure 5: *Black hole shadows with varying spin (left panel) and varying observer's inclination angle (right panel), as seen by a distant observer. The black hole shapes were numerically computed by reverse ray tracing from the observer to the black hole, noting the boundary between captured and escaping photons for an observer placed at a distance* $r = 1000\, r_{\mathrm{g}}$ *away from the black hole.*

The Black Hole Accretion Code (BHAC) is used to produce the Kerr black hole accretion simulation (Porth et al., 2017). Similar to the discussion in Section 2, the BHAC code solves equations of ideal GRMHD in arbitrary spacetime geometries using a more refined and efficient finite volume method. Since photons travel along null geodesics of the spacetime geometry, producing images of the black hole requires solving geodesic equations of motion in tandem with the radiative transfer equation (e.g., Younsi, Wu, and Fuerst, 2012). The images of Kerr black holes in this section are created using the GRRT code BHOSS (Younsi, 2019). Each image represents a snapshot of the black hole accretion emission evaluated at time $t = 10^4\, M$ in the code units described in Section 3.3. The time is chosen to be long enough for the GRMHD simulation to have evolved into a quasi-stationary state. Variations in the flux with time are omitted for brevity and will be discussed in the MSc thesis.

There is a relationship between the observed flux with the spin and inclination angle, but the mean historical flux density from Sgr A* is observationally constrained as $F = 3.4 \pm 0.5$ Jy (Bower, 2015). The images shown in Fig. 6, and 7 have each been normalized to Sgr A*'s observed total flux by varying the mass accretion rate $\dot{M}_{\mathrm{cgs}}$, which is a free parameter in the modelling.

In Fig. 6, the effect of varying the observer's inclination angle is compared and the numerically calculated black hole shadow shape is outlined by the green dashed line. The spin was chosen to be $a = 0.9375$ to accentuate the asymmetric and non-circular black hole shadow shape as compared to a Schwarzschild black hole. The four inclination angles, θ_{obs}, range from 5° to 90° as indicated in the top left corner of each panel. The angle 0° is not shown because there is a polar singularity in the chosen coordinate system. In these images, the emission is approximately rotationally uniform when observed face-on down the black hole rotation axis. But as the inclination angle increases up to 90°, the emission of the accretion travelling toward the observer increases in intensity compared to the accretion flowing away from the observer. When the accreting material is flowing toward the observer, relativistic aberration causes photons to be emitted in the direction of travel, and the Doppler effect blue-shifts photons into higher energy. The opposite effect occurs for accreting material travelling away from the observer, where photons are emitted away from the observer's direction and red-shifted. The net result is that the flux ratio between the brighter and darker limbs of the black hole depend sensitively on the accreting material's relative velocity. The effect is maximal when observed edge-on at 90°, where the intensity of the darker limb is insignificant compared to that of the brighter limb, and the observed flux is dominated by gravitational lensing of the accretion emission. These black hole shadow images represent predictions of the image to be observed by the EHT, and are calculated by fitting the total flux at 230 GHz (EHT observing frequency) to the observed flux of Sgr A*.

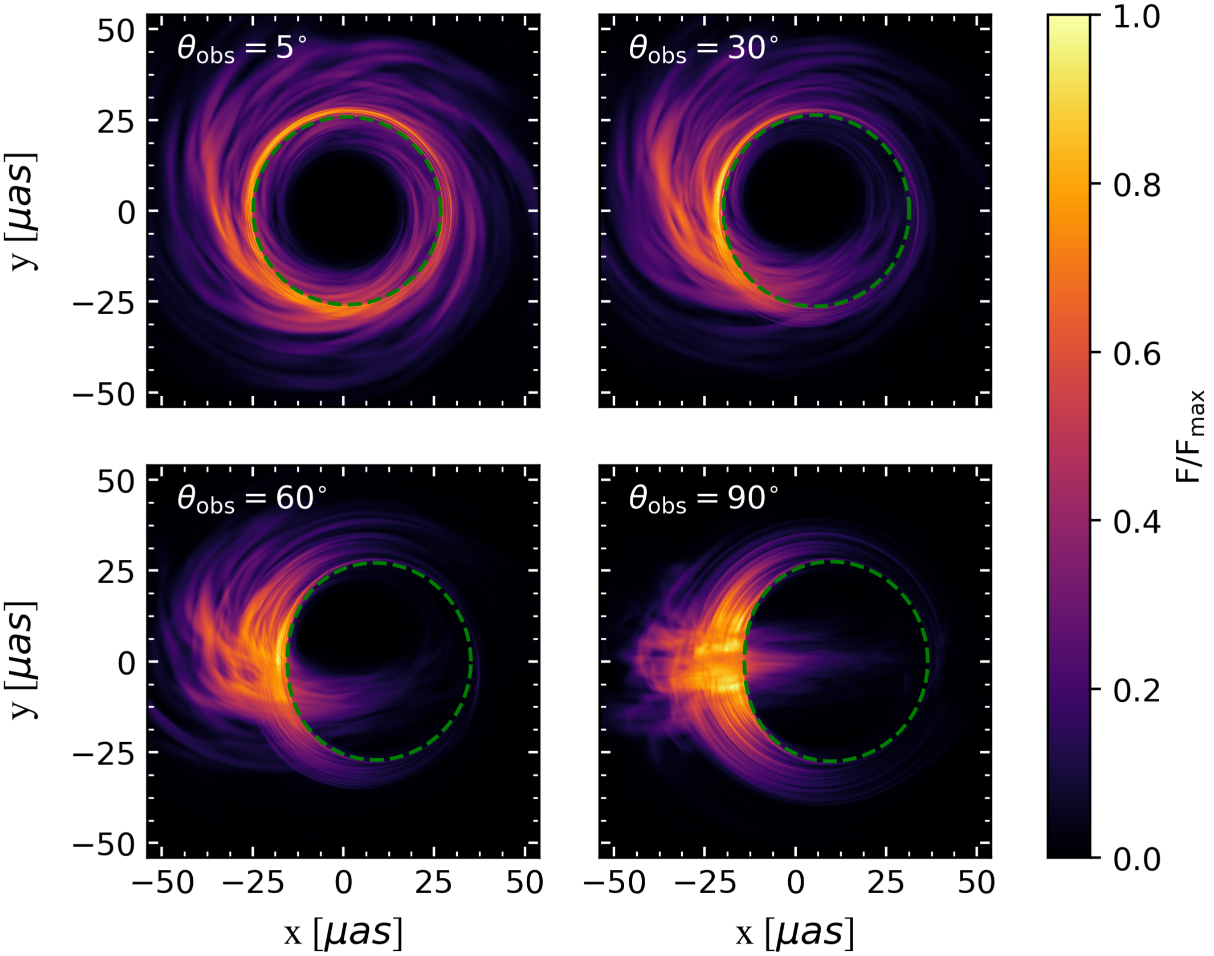

Figure 6: *Simulated Sgr A* images with spin* $a = 0.9375$ *and inclination angle ranging from* 5° *to* 90°*. The green dashed line denotes the black hole shadow boundary in vacuum. As will be shown in Section 4.2, the beam size is around* 26 µas*. These simulated images were created using BHAC code to evolve the accretion structure using GRMHD and BHOSS code to solve equations of GRRT.*

Negatively spinning (retrograde) black holes are predicted by AGN stochastic evolution models having antiparallel angular momenta between the black hole and its accretion disk, produced by misalignments which may have originated from the initial supernova kick (e.g., Dauser et al., 2011; Volonteri et al., 2005). Misaligned black holes eventually evolve to one of the parallel or antiparallel stable configurations of disk and black hole angular momentum; the re-alignment of the black hole with its accretion disk is thought to be governed by the Bardeen-Petterson effect (Bardeen and Petterson, 1975).

In the case of negatively spinning black holes, the intrinsic size of the accretion flow is expanded to more than twice as large as the images for black holes with positive spin (prograde). One of the reasons is that the radius of the ISCO, which denotes the inner boundary of the accretion disk, has increased out to $r_{\rm ISCO} \approx 8.8\ r_{\rm g}$ corresponding to ~47 arcseconds according to eqn. (16) for Sgr A*.

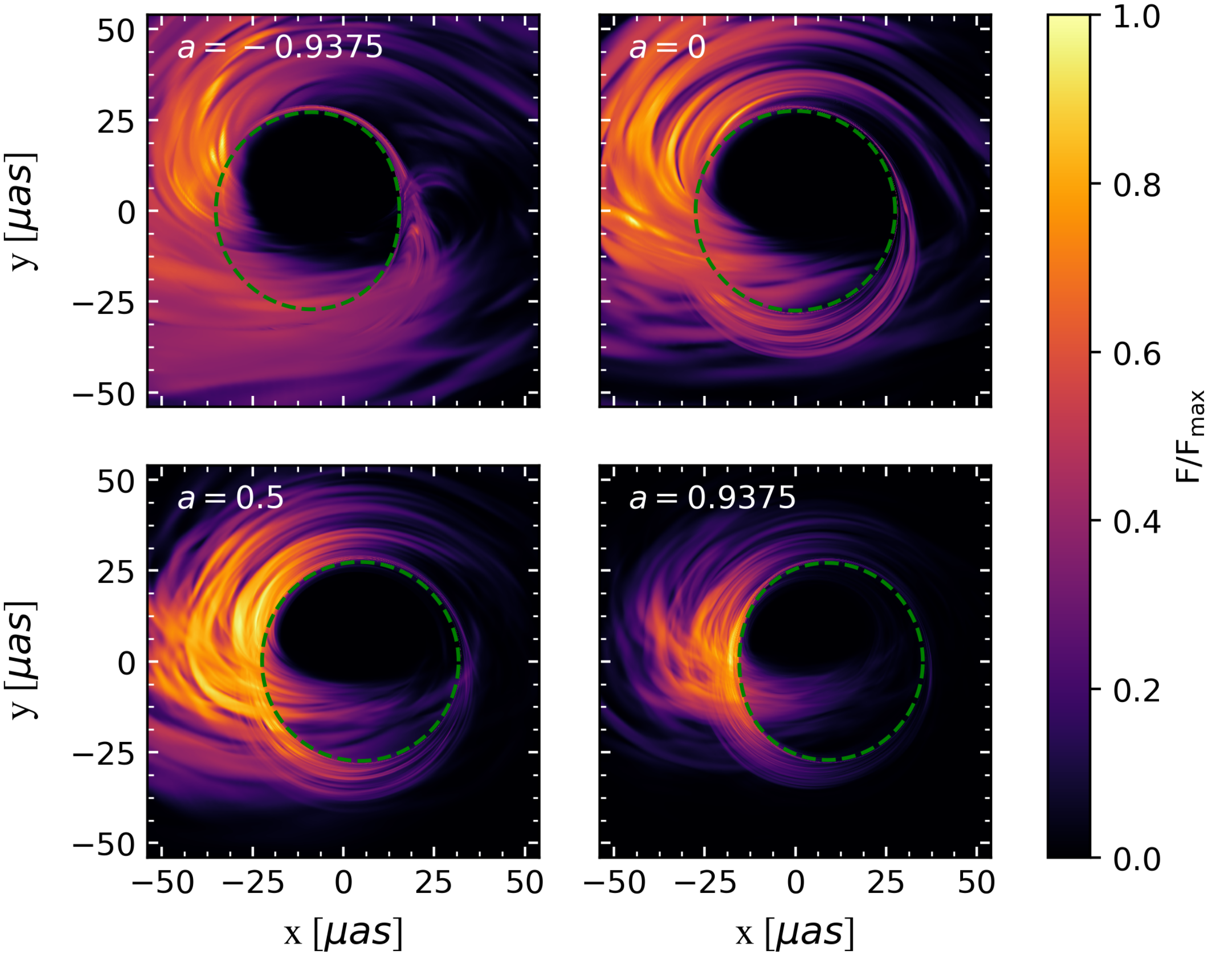

Figure 7: *Simulated Sgr A* images with varying spin parameter. The inclination angle is set to* $\theta = 60°$ *for all four panels. The shape of the black hole shadow becomes more asymmetric as the spin* $|a|$ *tends to 1. These simulated images were created using BHAC code to evolve the accretion structure using GRMHD and BHOSS code to solve equations of GRRT.*

By visualising the images obtained from varying the spin parameter for a fixed inclination angle as in Fig. 7, black holes of drastically different spins can be compared directly. Qualitatively, the images appear similar which may lead to a degeneracy in the measurement of spin as will be discussed in Section 4.3. However, the shape of the black hole shadow varies with spin. Furthermore, the ratio of the flux from the brighter and darker limbs of the black hole changes as well, where this difference is more pronounced for higher spin parameters. The scale of the emission also differs between spin parameters where the images for the negative spin and zero spin have much larger emission regions compared to the images for positively spinning accretion flow.

4.2 Observing the Black Hole

Very-Long Baseline Interferometry

The EHT employs sub-millimeter very-long baseline interferometry (VLBI) by taking data from an array of independent radio observatories around the world to create a single higher resolution image. Observations are made in the radio 230 GHz frequency band coinciding with the frequency at which the source, Sgr A*, is optically thin. In addition, its flux density as shown in the SED, Fig. 8, is close to its maximum. Furthermore, the 230 GHz frequency is located in the high atmospheric transmission regime called the radio window (Schieven, 2018). For these reasons, the 230 GHz frequency band used for the EHT observations is ideal for observing Sgr A*.

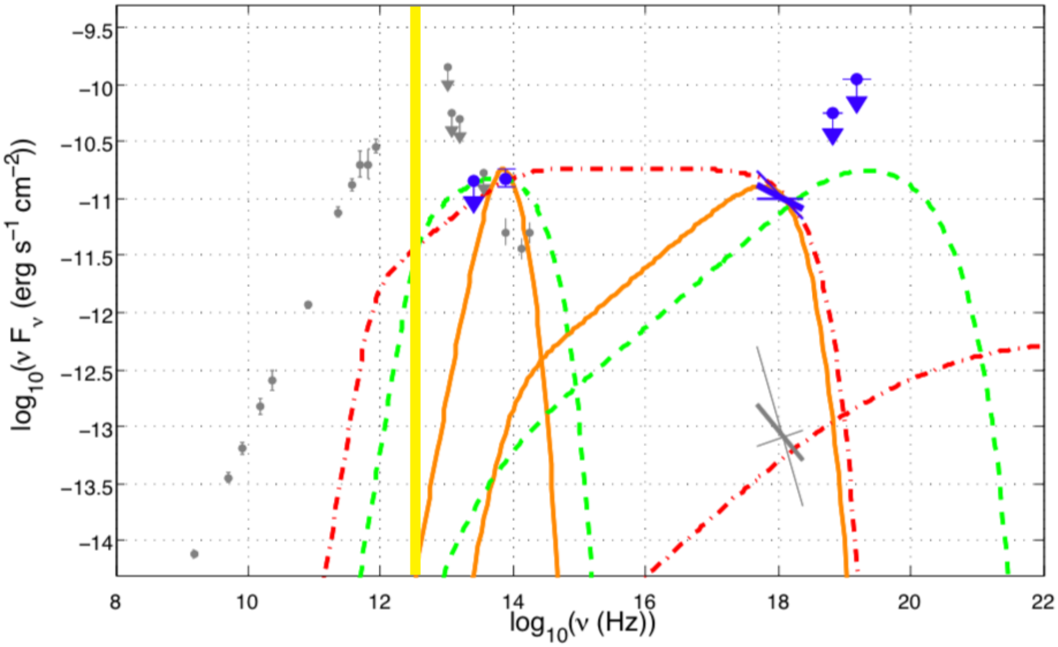

Figure 8: *The SED of Sgr A*, where the highlighted column indicates the position of the VLBI 230 GHz observing frequency, which is close to the flux maximum. The orange solid lines, green dashed lines, and red dash dotted lines represent the contributions of the synchrotron self-Compton, external Compton, and synchrotron broken power-law radiation processes respectively. The figure was obtained from Trap et al., 2010.*

In Fig. 8, the grey measurements are associated with the quiescent state. The VLBI observation wavelength band is targeted in this region where the flux is close to the maximum value, and where there are upper-limit measurements in the far-infrared and mid-infrared. The quiescent luminosity of Sgr A* is approximately ten orders of magnitude below the Eddington luminosity. This low luminosity may be a result of a low accretion rate and an accretion flow which is radiatively inefficient. The blue points are upper-limit measurements provided by the Very Large Telescope and the International Gamma-ray Astrophysics Laboratory. The blue X-ray bow-tie measurements indicate the slope of the SED (Trap et al., 2010).

The contribution to the SED from synchrotron self-Compton, external Compton, and synchrotron broken power-law radiation processes are modelled in Fig. 8. Synchrotron self-Compton, indicated by the solid orange lines, is an effect which is produced when electrons scatter their own synchrotron emission. Since all systems producing synchrotron radiation are up-scattered by their own electron population, synchrotron self-Compton is an important process for a self-consistent treatment of the accretion emission in strong magnetic fields. The three models together provide a good fit for the flaring in the higher frequency regime of the SED (Trap et al., 2010).

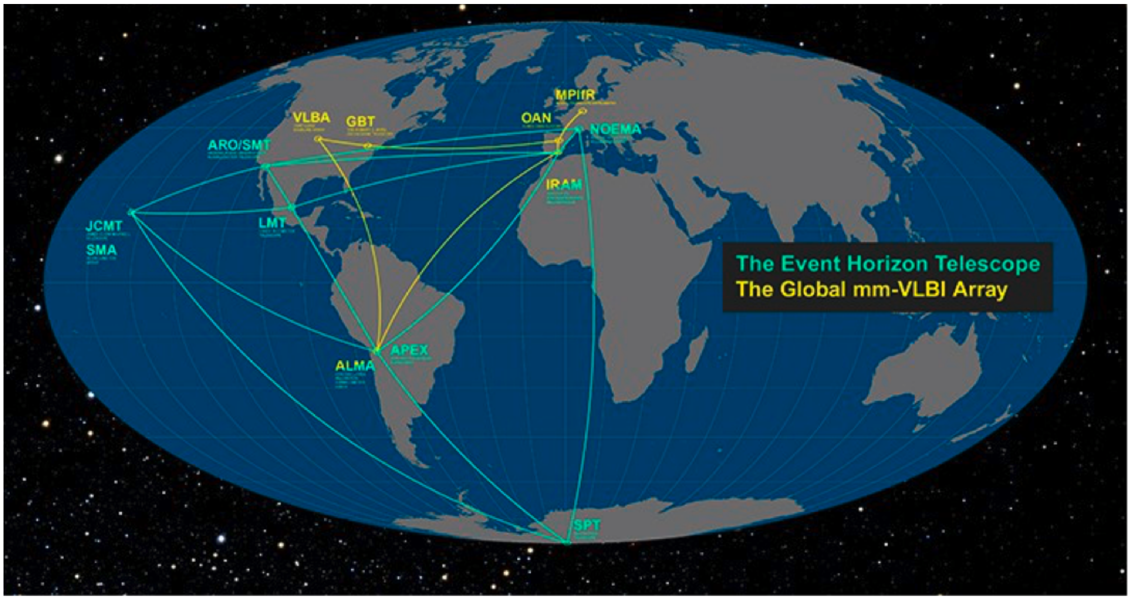

Figure 9: *Map of EHT array sites. Credit: EHT Collaboration, https://eventhorizontelescope.org/science.*

In VLBI, each of the telescopes are directed towards the target and synchronised using precise atomic clocks. Data representations of an image are collected in Fourier space. Large volumes of data in hard drives are shipped from the various telescopes to MIT Haystack Observatory and Max Planck Institute for Radio Astronomy. At these locations, the data is cross-correlated together to reconstruct an image. The real image will be contaminated by various effects from interstellar medium scattering, atmospheric scattering, and turbulence, but certain pipelines and data from models of the interstellar medium can be used to correct for these effects (Bouman et al., 2016; Johnson et al., 2017). The EHT array shown in Fig. 9 is composed of a global network of radio observatories in many countries located in the Northern and Southern Hemispheres. By increasing the baseline distance, the EHT simulates a telescope with an effective diameter of the order of the Earth's diameter.

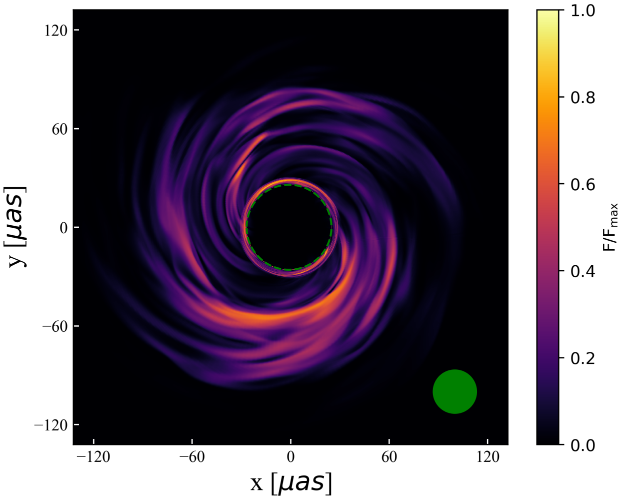

Figure 10: *Plot of the VLBI best resolution beam size compared to a simulated image of Sgr A* with spin parameter* $a = -15/16$ *and observer's inclination angle* $\theta = 5°$. *The beam is represented by the filled green circle with a* $26\,\mu$as *radius.*

Located 26,000 light years away from the Earth, imaging Sgr A* on event horizon scales requires an angular resolution $R \approx 53\,\mu$as. The resolution of a telescope is proportional to the wavelength of observation and the size of the telescope $R = k\lambda/D$, where λ is the wavelength, D is the diameter of the telescope, and k has a value of 1.22 for diffraction through a circular aperture. The maximum theoretical resolution of EHT at 230 GHz can be approximated by considering $D \approx 12,742\,\mathrm{km}$, the Earth's diameter. The best resolution at 230 GHz is then $R \approx 26\,\mu\mathrm{as}$ [1], enough to observe not only Sgr A* at 53 μas, but also the accretion disk around the supermassive black hole at the center of galaxy M87 where $R \approx 22\,\mu\mathrm{as}$. A comparison of this beam size with a negatively spinning black hole is shown in Fig. 10, where the beam is approximated as circular with a diameter of $26\,\mu$as. As seen in Fig. 9, the maximum baseline distances differ between the North-South and East-West cardinal directions, where longer baselines can resolve smaller scale structures. Therefore, the real observing beam is elliptical rather than perfectly circular. Moreover, measurements obtained from observing an object as the Earth rotates over the course of a day form elliptical tracks in the image's spatial frequency plane (Bouman et al., 2016). In all, taking into account telescope resolution from VLBI and correcting for scatter broadening from the interstellar medium, there is a strong expectation that Sgr A* can be directly imaged (Falcke, Melia, and Agol, 2000).

Image Reconstruction

Image reconstruction from data obtained by the VLBI telescope array presents a number of challenges. By nature, the data is extremely sparse with low spatial frequency coverage compared to a telescope with a disk size of the Earth's diameter, which the EHT is simulating. Furthermore, the time delay between photons obtained by telescopes in the array must be accounted for, so all the telescopes are synchronised with precise atomic clocks. Despite this, inhomogeneities in the atmosphere introduce noise and delays in the light speed which affects the phase of measurements. There is also an infinite number of possible images which fit the data, so some assumptions must be made about what a reasonable image should look like. To tackle these challenges, an algorithm called CHIRP was developed in 2016 using a Bayesian approach which has demonstrated good results with low signal-to-noise ratio (SNR) and extended emission in publicly available data and synthetic experiments. The algorithm parameterises the resulting continuous image with a discrete number of terms, accounts for a Gaussian noise distribution, and incorporates an iterative optimization framework for energy minimization, called the maximum entropy method (MEM) (Bouman et al., 2016).

4.3 Measuring the Black Hole Spin

One of the established ways of measuring the black hole spin is by the continuum-fitting method. Because the radius of the ISCO is highly dependent on spin as well as prograde or retrograde rotation, fitting the X-ray continuum spectrum of the black hole emission can provide an estimate for the inner edge of the accretion disk. Assuming a sharp truncation of the accretion disk at the ISCO radius, the method works by fitting the broadband X-ray continuum, including relativistic, self-irradiation, limb-darkening, and Comptonization contributions (McClintock et al., 2011). However, the limitations are that accurate measurements of the distance d to the source, mass M of the black hole, and inclination θ_{obs} of the accretion disk must be firmly established beforehand. In addition, the observed flux F_{obs} emitted locally by the disk has to be obtained, presenting observational challenges such as maintaining high SNR, subtracting contamination by other sources, consideration of flux diminution by the intergalactic or interstellar medium, etc. For these reasons, it is useful to develop an independent way of measuring black hole spin from direct imaging of the black hole shadow. In theory, because the shape of the black hole shadow depends sensitively on the spin parameter, it is possible to infer the spin from the shape of the shadow. In practice, the inclination angle is a confounding variable resulting in observational degeneracies where images of vastly different spin can appear similar in shape if the inclination angle is adjusted to compensate.

One of the ways to measure spin from the black hole shadow is to introduce an observable bisector axis named the *shadow axis*. The shadow axis is defined as the bisector perpendicular to the axis of the black hole shadow's maximum width (Takahashi, 2004). This shadow axis is defined for the observer, so its position can easily be determined from observations of black holes with accretion disks. The minimum distance between the mass center of the black hole and the shadow axis is strongly dependent on the spin parameter. Thus as long as the black hole shadow is observed and the mass center is known, it is possible to measure the black hole's spin parameter.

---

[1] The angular resolution is comparable to observing an orange on the surface of the moon with the naked eye.

In Section 4.2, the feasibility of observing a black hole shadow using VLBI was established. With regards to determining the position of the black hole mass center, there are various methods for Sgr A*. Since Sgr A* in the Galactic Center is close enough to the Earth to resolve stellar orbital trajectories, the position of the mass center can be measured by observing stellar motions around the black hole. Measurements of the black hole accretion disk brightness distribution can also be used to constrain the position of the center of mass by comparing the observations against models such as the calculations made by Luminet (Luminet, 1979). However, parameters of the fit include not only the position of the mass center, but also position and orientation of the rotation axis. If the rotation axis can be determined, axis ratios between the vertical extent and the width of the black hole is an indicator for the magnitude of the spin. This calculation may be performed by fitting the shadow with a circle of radius $R_{\rm s}$ using three points as a first approximation, and then defining a distortion parameter $\delta_{\rm s} \equiv D_{\rm cs}/R_{\rm s}$, where $D_{\rm cs}$ is the difference between the maximally "dented" side of the observed shadow with the circle approximation (Li and Bambi, 2014). Because the dent is more pronounced for greater spin, the distortion parameter can be an indicator for the black hole spin. From the Luminet calculations, the best-fit parameters may be used to measure the black hole spin with the shadow axis and the mass center, or the position of the rotation axis may also be used to determine spin.

Although there are degeneracies in the inclination and spin parameters when observing extragalactic SMBH, the situation is different for Sgr A* due to its relative proximity to Earth. Specifically for observing Sgr A*, the inclination angle between its rotation axis and the observation from Earth is expected to be constrained within 45° and 135°, because the solar system lies in the thin disk of the Milky Way and the SMBH in the Galactic Center is expected to share the overall angular momentum of the Milky Way. Measurements made of Sgr A*'s mass from stellar orbits and distance measurements fix the expected angular size of its black hole shadow, because the angular size of the shadow depends entirely on the black hole mass and distance to the source. From Fig. 5, when the mass and distance are fixed, measuring the size of the black hole shadow can be used to determine the observation inclination angle more precisely. Therefore, if the inclination angle can be measured, the spin can be estimated from the Sgr A* black hole shadow asymmetry by fitting a model of the shadow shape, varying the spin for a fixed inclination angle. Using these methods, there is a reasonable expectation that the image of the Sgr A* shadow can be used to estimate the black hole's spin parameter.

5 Remarks and Conclusion

Using self-consistent numerical simulations involving GRMHD and GRRT, this research essay presents realistic representations of the dynamical and turbulent nature of accretion flow around Kerr black holes. It was shown that the shape of the black hole shadow has strong dependencies on the black hole spin and observer's inclination angle, such that a direct image of black hole accretion is a potential source of information for investigating the black hole's physical characteristics. Real images of the black hole shadow are obfuscated by scattering from the interstellar medium and atmospheric turbulence. Observing Sgr A* through the galactic disk introduces a large column density of particles which influence the observed image. However, models which can correct for these effects are considered during image reconstruction. Convolving the simulated image with the elliptical VLBI beam provides a realistic prediction of the observation in the correct resolution. When the real image of the Sgr A* black hole shadow is released, it is possible to compare the result with simulated images to better constrain black hole mass and spin. Furthermore, the black hole shadow may offer another method for testing general relativity against alternative theories of gravity.

The thesis project which follows this essay will investigate the effects of varying the electron distribution function and proton-electron temperature coupling on the accretion dynamics at the edge of the black hole event horizon. With the GRMHD and GRRT simulations used in this report, the project will also investigate time variability and temporal spectral variations of the emission from the accretion in-flow. The relationship between the mass accretion rate and the total flux of accretion emission will also be discussed in greater detail. Furthermore, realistic predictions of the obfuscated image including effects of interstellar scattering and the image reconstruction process will be compared to the real image to be published in April 2019.

References

Abbott, B. P. et al. (2016). “Observation of Gravitational Waves from a Binary Black Hole Merger”. In: *Phys. Rev. Lett.* 116.6, p. 061102. DOI: `10.1103/PhysRevLett.116.061102`. arXiv: `1602.03837 [gr-qc]`.

Abdujabbarov, A. A., L. Rezzolla, and B. J. Ahmedov (2015). “A coordinate-independent characterization of a black hole shadow”. In: *Mon. Not. Roy. Astron. Soc.* 454.3, pp. 2423–2435. DOI: `10.1093/mnras/stv2079`. arXiv: `1503.09054 [gr-qc]`.

Abramowicz, Marek A. and P. Chris Fragile (2013). “Foundations of Black Hole Accretion Disk Theory”. In: *Living Rev. Rel.* 16, p. 1. DOI: `10.12942/lrr-2013-1`. arXiv: `1104.5499 [astro-ph.HE]`.

Balbus, S. A. and J. F. Hawley (July 1991). “A powerful local shear instability in weakly magnetized disks. I - Linear analysis. II - Nonlinear evolution”. In: *Astrophysical Journal* 376, pp. 214–233. DOI: `10.1086/170270`.

Bardeen, J. M. and J. A. Petterson (Jan. 1975). “The Lense-Thirring Effect and Accretion Disks around Kerr Black Holes”. In: *Astrophysical Journal, Letters* 195, p. L65. DOI: `10.1086/181711`.

Bardeen, J. M., W. H. Press, and S. A. Teukolsky (Dec. 1972). “Rotating Black Holes: Locally Nonrotating Frames, Energy Extraction, and Scalar Synchrotron Radiation”. In: *Astrophysical Journal* 178, pp. 347–370. DOI: `10.1086/151796`.

Bian, Wei-Hao and Yong-Heng Zhao (2003). “Accretion rates and accretion efficiency in agns”. In: *Submitted to: Publ. Astron. Soc. Jap.* arXiv: `astro-ph/0305095 [astro-ph]`.

Blandford, R. D. and R. L. Znajek (May 1977). “Electromagnetic extraction of energy from Kerr black holes”. In: *Monthly Notices of the RAS* 179, pp. 433–456. DOI: `10.1093/mnras/179.3.433`.

Bouman, Katherine L. et al. (Mar. 2016). “Computational Imaging for VLBI Image Reconstruction”. In: *The IEEE Conference on Computer Vision and Pattern Recognition (CVPR*, p. 913. arXiv: `1512.01413 [astro-ph.IM]`.

Bower, Geoffrey C. et al. (2015). “Radio and Millimeter Monitoring of Sgr A*: Spectrum, Variability, and Constraints on the G2 Encounter”. In: *Astrophys. J.* 802.1, p. 69. DOI: `10.1088/0004-637X/802/1/69`. arXiv: `1502.06534 [astro-ph.HE]`.

Carter, B. (Oct. 1968). “Global Structure of the Kerr Family of Gravitational Fields”. In: *Physical Review* 174, pp. 1559–1571. DOI: `10.1103/PhysRev.174.1559`.

Chakraborty, Chandrachur, Prashant Kocherlakota, and Pankaj S. Joshi (2017). “Spin precession in a black hole and naked singularity spacetimes”. In: *Phys. Rev.* D95.4, p. 044006. DOI: `10.1103/PhysRevD.95.044006`. arXiv: `1605.00600 [gr-qc]`.

Cunningham, C. T. and J. M. Bardeen (July 1973). “The Optical Appearance of a Star Orbiting an Extreme Kerr Black Hole”. In: *Astrophysical Journal* 183, pp. 237–264. DOI: `10.1086/152223`.

Dauser, T. et al. (Feb. 2011). “Broad emission lines for a negatively spinning black hole”. In: *Jets at All Scales*. Ed. by G. E. Romero, R. A. Sunyaev, and T. Belloni. Vol. 275. IAU Symposium, pp. 100–101. DOI: `10.1017/S1743921310015735`.

D’Inverno, R. (1992). *Introducing Einstein’s Relativity*. Comparative Pathobiology - Studies in the Postmodern Theory of Education. Clarendon Press. ISBN: 9780198596868. URL: `https://books.google.co.uk/books?id=yqcT3VICuvMC`.

Dokuchaev, V. I. and N. O. Nazarova (2018). “Event horizon image within black hole shadow”. In: arXiv: `1804.08030 [astro-ph.HE]`.

Einstein, A. (1916). “Die Grundlage der allgemeinen Relativitätstheorie”. In: *Annalen der Physik* 354, pp. 769–822. DOI: `10.1002/andp.19163540702`.

Falcke, H., F. Melia, and E. Agol (Jan. 2000). “Viewing the Shadow of the Black Hole at the Galactic Center”. In: *Astrophysical Journal, Letters* 528, pp. L13–L16. DOI: `10.1086/312423`. eprint: `astro-ph/9912263`.

Fishbone, L. G. and V. Moncrief (Aug. 1976). “Relativistic fluid disks in orbit around Kerr black holes”. In: *Astrophysical Journal* 207, pp. 962–976. DOI: `10.1086/154565`.

Frank, J., A. King, and D. Raine (2002). *Accretion Power in Astrophysics*. Accretion Power in Astrophysics. Cambridge University Press. ISBN: 9780521629577. URL: `https://books.google.co.uk/books?id=GGM\_t-xn8ocC`.

Gammie, Charles F., Jonathan C. McKinney, and Gabor Toth (2003). “HARM: A Numerical scheme for general relativistic magnetohydrodynamics”. In: *Astrophys. J.* 589, pp. 444–457. DOI: `10.1086/374594`. arXiv: `astro-ph/0301509 [astro-ph]`.

Ghez, A. M. et al. (1998). “High proper motion stars in the vicinity of Sgr A*: Evidence for a supermassive black hole at the center of our galaxy”. In: *Astrophys. J.* 509, pp. 678–686. DOI: `10.1086/306528`. arXiv: `astro-ph/9807210 [astro-ph]`.

Goddi, C. et al. (2016). “BlackHoleCam: Fundamental physics of the galactic center”. In: *Int. J. Mod. Phys.* D26.02. [1,863(2017)], p. 1730001. DOI: `10.1142/S0218271817300014,10.1142/9789813226609_0046`. arXiv: `1606.08879 [astro-ph.HE]`.

Grenzebach, Arne, Volker Perlick, and Claus Lämmerzahl (2014). “Photon Regions and Shadows of Kerr-Newman-NUT Black Holes with a Cosmological Constant”. In: *Phys. Rev.* D89.12, p. 124004. DOI: `10.1103/PhysRevD.89.124004`. arXiv: `1403.5234 [gr-qc]`.

Issaoun, S. et al. (2019). “The Size, Shape, and Scattering of Sagittarius A* at 86 GHz: First VLBI with ALMA”. In: *Astrophys. J.* 871.1, p. 30. DOI: `10.3847/1538-4357/aaf732`. arXiv: `1901.06226 [astro-ph.HE]`.

Johnson, Michael D. et al. (2017). “Dynamical Imaging with Interferometry”. In: *Astrophysical Journal* 850, 172, p. 172. DOI: `10.3847/1538-4357/aa97dd`. arXiv: `1711.01286 [astro-ph.IM]`.

Kerr, Roy P. (1963). “Gravitational Field of a Spinning Mass as an Example of Algebraically Special Metrics”. In: *Phys. Rev. Lett.* 11 (5), pp. 237–238. DOI: `10.1103/PhysRevLett.11.237`. URL: `https://link.aps.org/doi/10.1103/PhysRevLett.11.237`.

Li, Zilong and Cosimo Bambi (2014). “Measuring the Kerr spin parameter of regular black holes from their shadow”. In: *JCAP* 1401, p. 041. DOI: `10.1088/1475-7516/2014/01/041`. arXiv: `1309.1606 [gr-qc]`.

Luminet, J.-P. (May 1979). “Image of a spherical black hole with thin accretion disk”. In: *Astronomy and Astrophysics* 75, pp. 228–235.

McClintock, Jeffrey E. et al. (2011). “Measuring the Spins of Accreting Black Holes”. In: *Class. Quant. Grav.* 28, p. 114009. DOI: `10.1088/0264-9381/28/11/114009`. arXiv: `1101.0811 [astro-ph.HE]`.

Mizuno, Yosuke et al. (2018). “The Current Ability to Test Theories of Gravity with Black Hole Shadows”. In: *Nat. Astron.* 2.7, pp. 585–590. DOI: `10.1038/s41550-018-0449-5`. arXiv: `1804.05812 [astro-ph.GA]`.

Morgan, C. W. et al. (July 2007). “The Quasar Accretion Disk Size - Black Hole Mass Relation”. In: *ArXiv e-prints*. arXiv: `0707.0305`.

Penrose, R and R M. Floyd (Feb. 1971). “Extraction of Rotational Energy from a Black Hole”. In: *Nature* 229, pp. 177–179. DOI: `10.1038/physci229177a0`.

Porth, O. et al. (May 2017). “The black hole accretion code”. In: *Computational Astrophysics and Cosmology* 4, 1, p. 1. DOI: `10.1186/s40668-017-0020-2`. arXiv: `1611.09720 [gr-qc]`.

Repin, S. V. et al. (Feb. 2018). “Shadow of rotating black holes on a standard background screen”. In: *ArXiv e-prints*. arXiv: `1802.04667 [gr-qc]`.

Rosquist, Kjell, Tomas Bylund, and Lars Samuelsson (2009). “Carter’s constant revealed”. In: *Int. J. Mod. Phys.* D18, pp. 429–434. DOI: `10.1142/S0218271809014546`. arXiv: `0710.4260 [gr-qc]`.

Rybicki, G. B. and A. P. Lightman (June 1986). *Radiative Processes in Astrophysics*, p. 400.

Schieven, G. (2018). “Observing with ALMA - a Primer”. In: 1.

Schwarzschild, K. (1916). “On the Gravitational Field of a Mass Point According to Einstein’s Theory”. In: *Abh. Konigl. Preuss. Akad. Wissenschaften Jahre 1906,92, Berlin,1907* 1916.

— (1999). “On the gravitational field of a mass point according to Einstein’s theory”. In: *arXiv e-prints*, physics/9905030, physics/9905030. arXiv: `physics/9905030 [physics.hist-ph]`.

Shaikh, Rajibul et al. (2019). “Shadows of spherically symmetric black holes and naked singularities”. In: *Mon. Not. Roy. Astron. Soc.* 482, p. 52. DOI: `10.1093/mnras/sty2624`. arXiv: `1802.08060 [astro-ph.HE]`.

Takahashi, R. (Aug. 2004). “Shapes and Positions of Black Hole Shadows in Accretion Disks and Spin Parameters of Black Holes”. In: *Astrophysical Journal* 611, pp. 996–1004. DOI: `10.1086/422403`. eprint: `astro-ph/0405099`.

Thirring, H. (1918). “Über die Wirkung rotierender ferner Massen in der Einsteinschen Gravitationstheorie.” In: *Physikalische Zeitschrift* 19.

Trap, G. et al. (2010). “Soft gamma-ray constraints on a bright flare from the Galactic Center supermassive black hole”. In: *Advances in Space Research* 45, pp. 507–520. DOI: `10.1016/j.asr.2009.09.025`. arXiv: `0910.0399 [astro-ph.HE]`.

Visser, Matt (2007). “The Kerr spacetime: A Brief introduction”. In: *Kerr Fest: Black Holes in Astrophysics, General Relativity and Quantum Gravity Christchurch, New Zealand, August 26-28, 2004*. arXiv: `0706.0622 [gr-qc]`.

Volonteri, M. et al. (Feb. 2005). “The Distribution and Cosmic Evolution of Massive Black Hole Spins”. In: *Astrophysical Journal* 620, pp. 69–77. DOI: `10.1086/426858`. eprint: `astro-ph/0410342`.

Younsi Z., et. al. (2019). “Dynamical Covariant General-Relativistic Radiative Transfer”. In:

Younsi, Z., K. Wu, and S. V. Fuerst (Sept. 2012). “General relativistic radiative transfer: formulation and emission from structured tori around black holes”. In: *Astronomy and Astrophysics* 545, A13, A13. DOI: `10.1051/0004-6361/201219599`. arXiv: `1207.4234 [astro-ph.HE]`.

Yuan, Feng and Ramesh Narayan (2014). “Hot Accretion Flows Around Black Holes”. In: *Ann. Rev. Astron. Astrophys.* 52, pp. 529–588. DOI: `10.1146/annurev-astro-082812-141003`. arXiv: `1401.0586 [astro-ph.HE]`.